energies

MDPI

Article

Structural, Optical, and Magnetic Properties of Cobalt-Doped $ZnAl_2O_4$ Nanosheets Prepared by Hydrothermal Synthesis

Thirumala Rao Gurugubelli [1], Bathula Babu [2,*] and Kisoo Yoo [2,*]

[1] Physics Division, Department of Basic Sciences and Humanities, GMR Institute of Technology, GMR Nagar, Rajam 532127, India; Thirumala.phy@gmail.com
[2] School of Mechanical Engineering, Yeungnam University, Gyeongsan 712-749, Korea
* Correspondence: babu.physicist@gmail.com (B.B.); kisooyoo@yu.ac.kr (K.Y.)

Abstract: Nanomaterials with collective optical and magnetic properties are called smart or functional materials and have promising applications in many fields of science and technology. Undoped and Co-doped $ZnAl_2O_4$ were prepared using a co-precipitation-assisted hydrothermal method. A systematic investigation was carried out to understand the effects of the Co concentration on the crystalline phase, morphology, and optical and magnetic properties of Co-doped $ZnAl_2O_4$. X-ray diffraction confirmed the cubic spinel structure with the Fd3m space group, and there was no impurity phase. X-ray photoelectron spectroscopy of Co-doped $ZnAl_2O_4$ confirmed the existence of Zn, Al and O, and the Co in the optimized sample of ZAO-Co-3 confirmed the oxidation state of cobalt as Co^{2+}. Transmission electron microscopy of pure and Co-doped $ZnAl_2O_4$ revealed micro-hexagons and nanosheets, respectively. The optical absorption results showed that the bandgap of $ZnAl_2O_4$ decreased with increasing Co concentration. The hysteresis loop of Co-doped $ZnAl_2O_4$ revealed clear ferromagnetic behavior at room temperature. The as-prepared materials are suitable for energy storage applications, such as in supercapacitors and fuel cells. This work aims to focus on the effect of cobalt ions in different concentrations on structural, optical and magnetic properties.

Keywords: $ZnAl_2O_4$; cobalt-doping; bandgap; optical; magnetic

check for updates

Citation: Gurugubelli, T.R.; Babu, B.; Yoo, K. Structural, Optical, and Magnetic Properties of Cobalt-Doped $ZnAl_2O_4$ Nanosheets Prepared by Hydrothermal Synthesis. *Energies* **2021**, *14*, 2869. https://doi.org/10.3390/en14102869

Academic Editor: Bashir A. Arima

Received: 8 April 2021
Accepted: 13 May 2021
Published: 16 May 2021

Publisher's Note: MDPI stays neutral with regard to jurisdictional claims in published maps and institutional affiliations.

Copyright: © 2021 by the authors. Licensee MDPI, Basel, Switzerland. This article is an open access article distributed under the terms and conditions of the Creative Commons Attribution (CC BY) license (https://creativecommons.org/licenses/by/4.0/).

1. Introduction

Over the past few decades, spinel-structured metal oxide nanomaterials have attracted considerable attention because of their unique crystal structure and optical properties [1–5]. Spinel semiconductors are comprised of a group of metal oxides having a chemical complex AB_2O_4, where A and B are di- and trivalent cations, respectively. Among the many spinel-based nanomaterials known, zinc aluminate ($ZnAl_2O_4$) has attracted interest owing to its utility in various fields, such as ceramics, sensors, catalysts, aerospace, lubricants, optical coatings, transparent conducting oxides (TCO), dielectrics, electronics, and optoelectronic devices [6–11]. $ZnAl_2O_4$ spinel is a natural mineral known as gahnite. $ZnAl_2O_4$ belongs to the Fd3m space group, having a cubic structure and wide bandgap of 3.8 eV. $ZnAl_2O_4$ has several advantages, such as high mechanical strength, high chemical and thermal stability, high quantum yields, and catalytic activity [12]. These advantages and the wide bandgap of $ZnAl_2O_4$ make it a potential candidate for numerous applications in materials science and technology [11]. The huge application potential of spinel $ZnAl_2O_4$ has prompted many studies on understanding and enhancing the fundamental properties.

Several investigations have reported that the incorporation of a transition metal or rare-earth element into the $ZnAl_2O_4$ spinel lattice enhances many important properties [6,13–16]. In particular, the optical properties of $ZnAl_2O_4$ spinel nanostructures may be improved by modifying the bandgap. The bandgap of $ZnAl_2O_4$ spinel can be tuned by the incorporation of transition metal ions with controllable optical properties, which offers superior potential applicability in optoelectronics [17]. Previous reports have shown that the optical properties of nanostructured materials depend strongly on the particle size,

crystal structure, morphology, uniform distribution of activators in the host lattice, and synthesis method [4,18–20]. Several approaches have been attempted for the synthesis of $ZnAl_2O_4$ spinel nanostructures, such as co-precipitation [21], solid-state reaction [22], microwave-assisted hydrothermal methods [23], and sol-gel [2,24–26], solvothermal [27], hydrothermal [5,28], solution combustion [4,29], and mechanical alloying methods [30]. Among these, the hydrothermal method is a suitable method for synthesizing $ZnAl_2O_4$ spinel nanostructures because of its high crystallinity, purity, and homogeneity. Moreover, the homogeneity of dopants in the spinel matrix improves the optical properties significantly. In this context, this study adopted a co-precipitated-assisted hydrothermal method for the synthesis of undoped and Co^{2+}-doped $ZnAl_2O_4$ spinel nanostructures. To better understand the effects of the dopant concentration on the size, optical, and magnetic properties of $ZnAl_2O_4$ spinel nanostructures, undoped and Co^{2+}-doped $ZnAl_2O_4$ spinel nanostructures were characterized using a range of spectroscopic techniques, such as X-ray diffraction (XRD), transmission electron microscopy (TEM), X-ray photoelectron microscopy (XPS), ultraviolet–diffuse reflectance spectroscopy (UV-DRS), and vibrating sample magnetometry (VSM).

2. Materials and Methods

All chemicals used in this experiment ($Zn(NO_3)_2$, $Al(NO_3)_3$, $Co(NO_3)_2{\cdot}6H_2O$, ethanol, ammonia (25%), deionized water) were analytical grade and used without further purification. All the chemicals were purchased from Sigma–Aldrich Co., Ltd., and the purity of all the chemicals was ≥98%. The samples of 0%, 1%, 3% and 5% Co-doped $ZnAl_2O_4$ nanostructures were prepared via the hydrothermal method. This involves the mixing of nitrate ions acting as oxidizing agents. $Zn(NO_3)_2.6H_2O$ (0.2 mol%) was dissolved in 20 mL of deionized water on a hot plate at 40 °C. $Al(NO_3)_3.9H_2O$ (0.4 mol%) was dissolved in 20 mL deionized water and stirred magnetically. Then, 20 mL of zinc solution was added dropwise to the aluminum solution with continuous stirring; 20 mL of $Co(NO_3)_2{\cdot}6H_2O$ solution (0.01, 0.03 and 0.05 mol%) was then added dropwise into the above mixture solution with continuous stirring for 20 min. After this, ammonia solution (25%) was added to the solution drop by drop by adjusting the pH to 9 and stirring for 60 min till a white precipitate occurred. The obtained solution was transferred into a Teflon-lined stainless steel autoclave and sealed tightly; then, it was introduce into a muffle furnace at 220 °C for 8 h. The white precipitate solution was washed and centrifuge thrice with deionized water, ethanol and water, respectively, then dried at 80 °C for 6 h. After drying, the resultant powder was annealed at 1000 °C for 5 h and ground manually in order to get fine particles. The obtained samples were named ZAO, ZAO-Co-1, ZAO-Co-3 and ZAO-Co-5, respectively. An undoped sample was prepared by the same procedure as above without cobalt nitrate, and the sample was named ZAO.

Powder XRD (Shimadzu 6100, Japan) patterns of the prepared samples were recorded using CuKα radiation. The surface morphology of the as-synthesized samples was examined by field emission scanning electron microscopy (FESEM, Hitachi, S-4800, Japan) and transmission electron microscopy (TEM; Hitachi, H-7600, Europe). The optical absorption spectra were obtained using a Cary 5000 UV–vis–NIR spectrophotometer. The elemental distribution and their oxidation states on the surface were examined by X-ray photoelectron spectroscopy (XPS; Thermo Scientific K-alpha, South Korea). The magnetic hysteresis loop was obtained via vibrating sample magnetometer (VSM; Lake Shore 7407, USA).

3. Results

3.1. XRD Analysis

Figure 1 shows the XRD patterns of $ZnAl_2O_4$ and $ZnAl_{2-x}Co_xO_4$ (x = 0.00, 0.01, 0.03 and 0.05) nanoparticles. The XRD pattern of $ZnAl_2O_4$ revealed peaks at 31.32°, 36.61°, 44.62°, 48.90°, 55.54°, 59.11°, 64.99°, 74.04°, and 77.17° 2θ, which were indexed to the (2 2 0), (3 1 1), (4 0 0), (3 3 1), (4 2 2), (5 1 1), (4 4 0), (6 2 0), and (5 3 3) crystal planes of the single-phase spinel $ZnAl_2O_4$, respectively. The XRD planes could be indexed to the

cubic spinel $ZnAl_2O_4$ phase (JCPDS file no.: 05-0669). No characteristic XRD peaks of any impurity phase, such as Co clusters or Co oxide, were observed, confirming the successful incorporation of doped Co^{2+} ions into the Zn^{2+} ion sites without distorting the crystal structure of zinc aluminate. The average crystalline size (D) was calculated using Scherrer's equation, $D = K\lambda/\beta \cos\theta$, where λ = wavelength of X-ray used, k = 0.9, and β = width at half maximum. The induced lattice strain was calculated using the expression $\varepsilon = \beta\cos\theta/4$. The lattice cell parameters and interplanar spacing were also calculated.

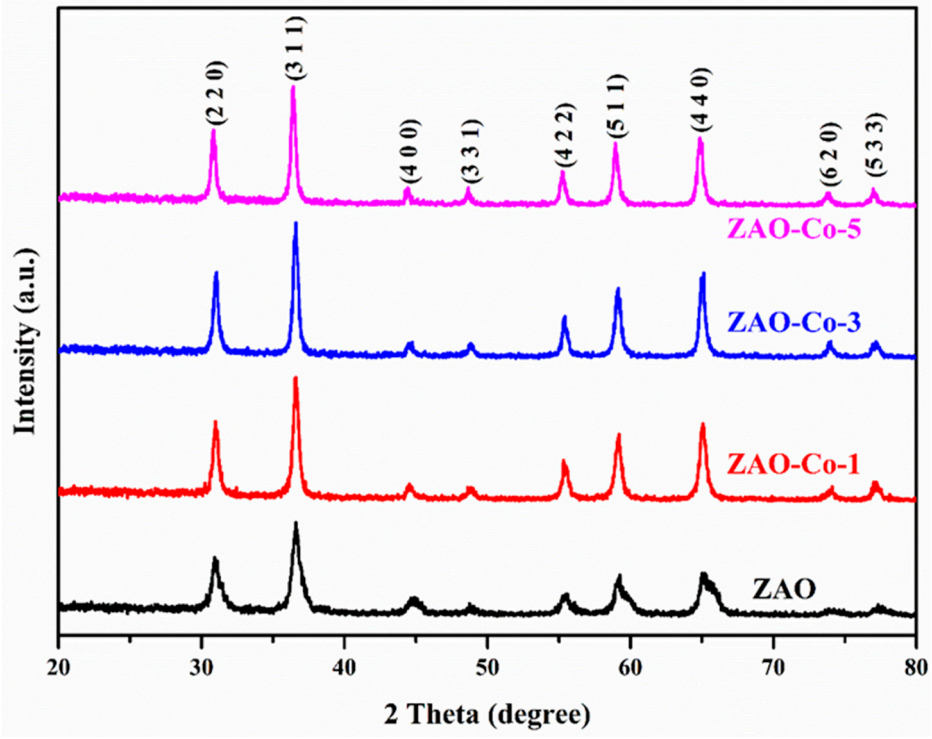


Figure 1. XRD patterns of pure ZAO and Co-doped ZAO nanosheets.

Table 1 lists the average crystallite size, lattice strain, lattice cell parameters, and interplanar spacing of $ZnAl_2O_4$ and Co-doped $ZnAl_2O_4$. The XRD peaks shifted slightly towards lower angles than the pure $ZnAl_2O_4$ (Figure 1). The interplanar spacing increased with a blue shift of the XRD angles, which may have arisen due to the smaller ionic radius of Co^{2+} (0.65 Å) than that of Zn^{2+} (0.74 Å). Moreover, a small positive shift in interatomic spacing and expansion in the lattice parameters occurred with increasing doping concentration. The average crystallite size of $ZnAl_2O_4$ shifted from 26 to 17 nm. The micro-strain of the $ZnAl_2O_4$ lattice increased with increasing Co doping concentration. Therefore, the particle size and lattice parameters can be controlled by the incorporation of foreign elements into the host lattice [26].

Table 1. Diffraction angles, lattice parameters, crystallite size, strain, and d-spacing values from XRD analysis.

Sample	Diffraction Angle (2θ)	Lattice Parameter (a = b = c) nm	Size (D) nm	Strain (ε) $\times 10^{-3}$	d-Spacing (nm)
ZAO	36.61	0.7574	26.6	1.304	0.2454
ZAO-Co-1	36.57	0.7572	23.6	1.467	0.2456
ZAO-Co-3	36.55	0.7577	21.3	1.629	0.2457
ZAO-Co-5	36.41	0.7591	17.7	1.955	0.2467

3.2. TEM Analysis

The morphology of ZAO and Co-doped ZAO nanosheets was examined by TEM, as shown in Figure 2. TEM of the pristine ZAO sample revealed a clear hexagon-shaped structure (Figure 2a). The ZAO hexagons showed slightly different sizes, but they were uniform in shape. Not all the sides of the hexagons were under 100 nm. Therefore, they can be considered micro hexagon structures. The reason behind the uniformity in shape might be the adopted hydrothermal procedure and the precursor concentration ratios.

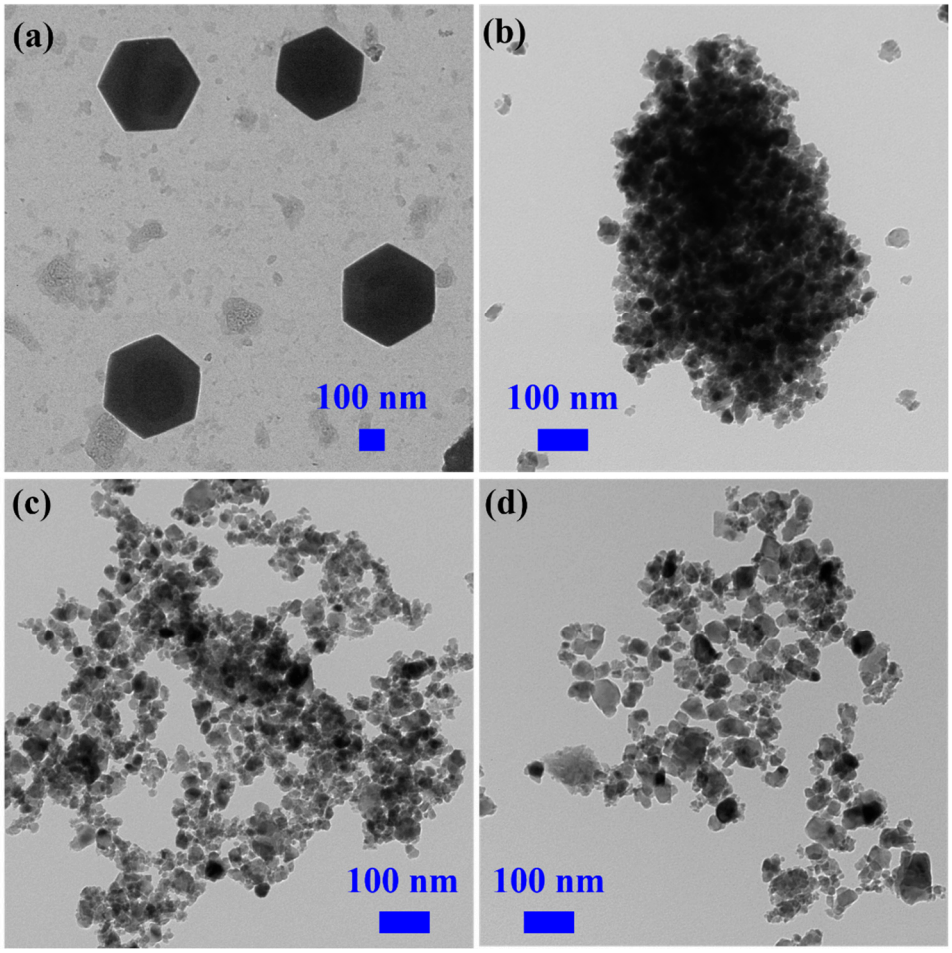


Figure 2. TEM images of (**a**) ZAO, (**b**) ZAO-Co-1, (**c**) ZAO-Co-3, and (**d**) ZAO-Co-5 nanosheets.

Cobalt doping into ZAO resulted in a significant modification of the morphology of ZAO. First, Co-doping changes the morphology from micro-hexagon structures to the nanoscale, as nanosheets. Second, the doping of cobalt disturbed the hexagon structure. This might be due to the successful doping of cobalt ions into the ZAO crystal lattice. All the Co-doped ZAO samples showed clear nanosheet-like morphologies compared to the undoped ZAO sample. Moreover, the increasing concentration of cobalt ions increases the distribution/separation of the nanosheets. The nanosheets of ZAO-Co-1 (Figure 2b) were densely packed to each other, but as the cobalt ion content increased further, the nanosheets were well separated, as observed in the case of ZAO-Co-3 and ZAO-Co-5 (Figure 2c,d). TEM confirmed that the doping of cobalt reduced the micro-hexagon structures to well-separated nanosheets.

3.3. XPS Analysis

XPS was applied to ZAO-Co-3 to evaluate the oxidation states and confirm the constituent elements of the prepared samples. Figure 3a provides details of the XPS survey

spectrum, confirming the existence of Zn, Al, O, and Co in the optimized sample of ZAO-Co-3. Figure 3b presents the high-resolution XPS spectrum of Zn. This spectrum showed two prominent XPS peaks at binding energies of 1021.66 and 1044.70 eV. These two peaks at 1021.66 and 1044.70 eV were assigned to Zn $2p_{3/2}$ and Zn $2p_{1/2}$, which confirmed the presence of Zn in the +2 oxidation state. The binding energy difference between Zn $2p_{3/2}$ and Zn $2p_{1/2}$ was 23.04 eV, confirming the presence of Zn^{2+} [31]. The XPS peak at 74.1 eV in Figure 3c was attributed to Al 2p. The oxidation state of Al was confirmed to be 3+, and these Al^{3+} cations were bonded to oxygen as Al-O [32]. Figure 3d shows the core-level XPS spectrum of O 1s with prominent and broad XPS peaks at 530.93 eV and a small intense peak at 532.81 eV. The O 1s peak at 530.93 was assigned to the contribution of oxygen and was attributed to Zn-O and Al-O bonds in the $ZnAl_2O_4$ lattice. The low intense XPS peak at 532.81 eV indicates an oxygen deficiency in the $ZnAl_2O_4$ crystal lattice [33], showing that some oxygen vacancies were present in the prepared samples. Figure 3e presents the high-resolution XPS spectrum of Co 2p, showing two major peaks at 781.2 and 796.43 eV, which were attributed to Co $2p_{3/2}$ and Co $2p_{1/2}$ eV, respectively [34]. In addition, two more satellite peaks were observed at approximately 786.75 and 802.73 eV. These outcomes confirm the presence of cobalt in mixed oxidation states of 2+ and 3+. The energy difference (ΔE) between Co $2p_{3/2}$ and Co $2p_{1/2}$ eV was 15.23 eV, which further confirmed the oxidation state of cobalt as Co^{2+}.

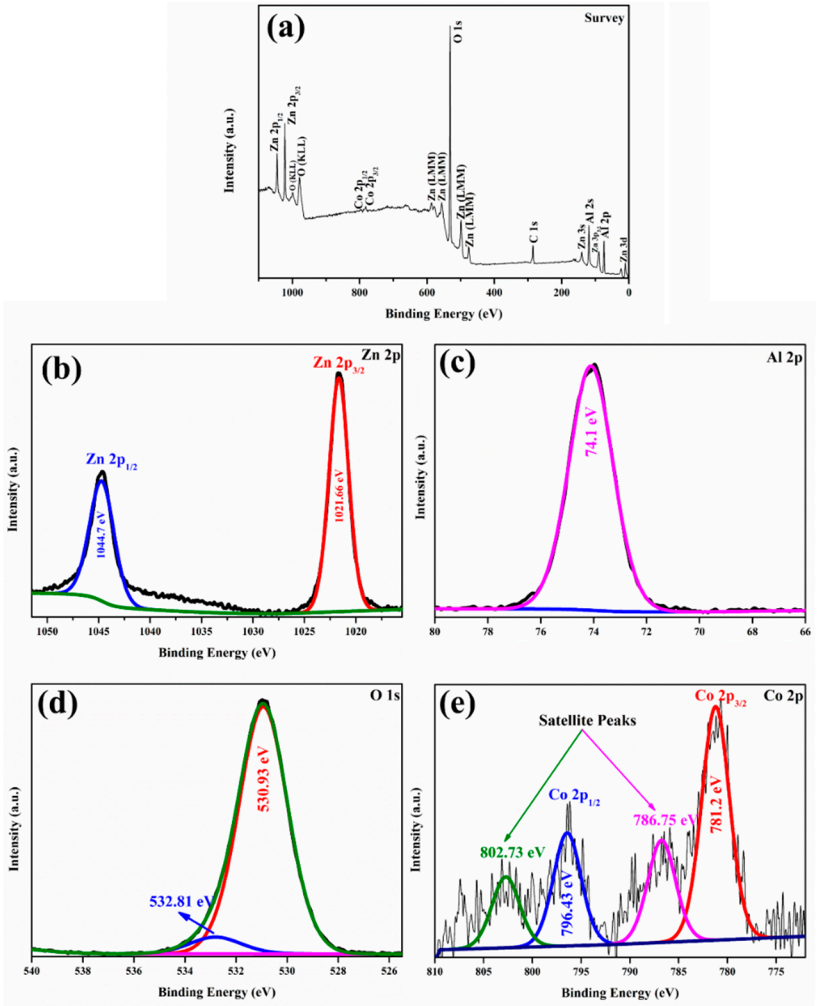


Figure 3. XPS spectra of ZAO-CO-3 nanosheets. (**a**) Survey, (**b**) Zn, (**c**) Al, (**d**) O, and (**e**) Co.

3.4. DRS Analysis

DRS, as shown in Figure 4, examined the optical properties of undoped ZAO and

Co-doped ZAO nanosheets. The optical absorption depends on many parameters, such as the bandgap, oxygen deficiency, and impurity centers. The bandgap of pristine ZAO was estimated to be 3.04 eV from its sharp absorption edge [35]. The doping of the ZAO matrix with cobalt ions causes changes in the optical properties of ZAO. The successful doping of Co^{2+} ions into the ZAO crystal system decreases the bandgap of ZAO with increasing cobalt content. The bandgaps of ZAO-Co-1, ZAO-Co-3, and ZAO-Co-5 were estimated to be 2.72, 2.37, and 2.23 eV, respectively. These bandgaps of the Co-doped samples were lower than the undoped ZAO sample, which was also expected due to the quantum limiting effect. The redshift in the bandgap of Co-doped ZAO was attributed to the sp-d interaction between the electrons in the band and local electrons in the d-shell of the substituted Co^{2+}. This may lead to a decrease in the conduction band potential and an increase in the valence band potential, leading to a decrease in bandgap [1]. In addition, the intensity of absorption increased with increasing Co content. The absorption edge of the Co-doped ZAO samples extended into the visible region. The new energy bands in the visible region arose due to the formation of new energy levels from Co ion-doping. The addition of energy bands in the visible region was assigned to the dopant Co ions as the inter-atomic d-d charge transfer of Co^{2+} cations [36]. The additional energy bands at approximately 406.6, 478.2, 546.5, and 620.7 nm were ascribed to $4T_{1g}(F) \rightarrow 2A_{1g}(G)$, $4T_{1g}(F) \rightarrow 4T_{1g}(G)$, $4T_{1g}(F) \rightarrow 4A_{2g}(F)$, and $4T_{1g}(F) \rightarrow 2T_{1g}(G)$ energy transitions, respectively [37]. These outcomes of bandgap reduction and addition energy bands in the visible region and the increased intensity of additional bands confirmed the successful doping of cobalt ions into the $ZnAl_2O_4$ crystal system.

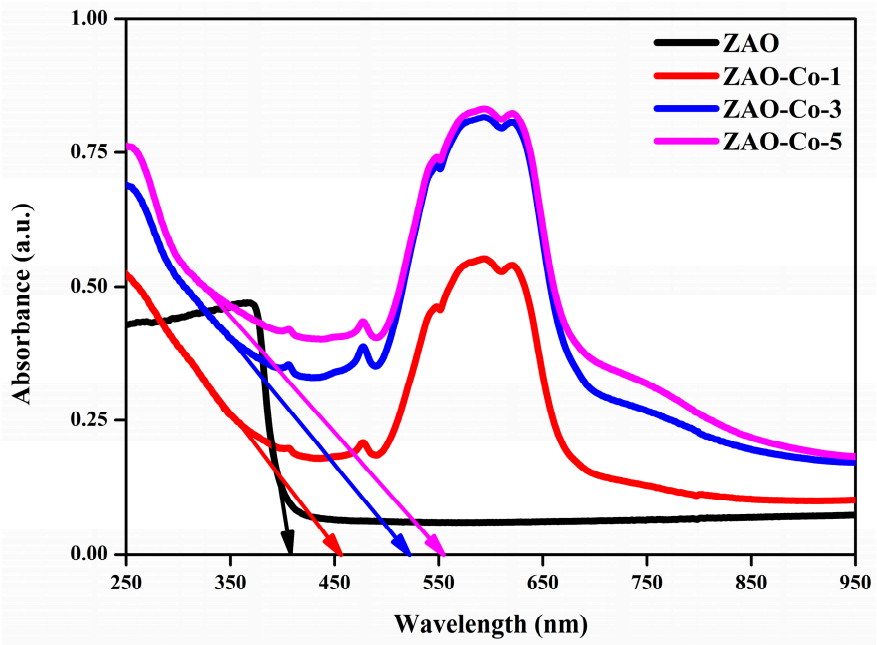


Figure 4. DRS spectra of ZAO and Co-doped ZAO nanosheets.

3.5. VSM Analysis

The magnetic behaviors of $ZnAl_2O_4$ and Co-doped $ZnAl_2O_4$ nanocrystals were investigated by VSM, as shown in Figure 5. Pure $ZnAl_2O_4$ nanocrystals showed no hysteresis loop, indicating its non-magnetic behavior [6]. On the other hand, the Co-doped $ZnAl_2O_4$ nanocrystals exhibited a clear ferromagnetic hysteresis at room temperature. Table 2 lists the saturation magnetization (Ms), retentivity (Mr), and coercive field (Hc) values. All Co-doped $ZnAl_2O_4$ nanocrystals exhibited a soft ferromagnetic nature with a low coercive field. The saturation magnetization and retentivity values increased gradually with increasing dopant concentration, and reached a maximum at ZAO-Co-3, then decreased with further increases in Co concentration. This indicates that most of the Co ions remain un-

coupled in ZAO-Co-5 and do not contribute to the ferromagnetic phase. The ferromagnetic behavior depends mainly on the Co dopant concentration. There are three main reasons for the ferromagnetism in the Co-doped $ZnAl_2O_4$ nanocrystals. One is the formation of a secondary phase, such as Co^{2+} clusters or oxides. XRD confirmed that Co^{2+} ions were incorporated into the $ZnAl_2O_4$ nanocrystals at the Zn^{2+} sites, and there was no possibility of secondary phase formation [38]. The second one is the carrier-induced ferromagnetism, i.e., the increase in free charge carriers due to the doping of Co2+ ions into ZnAl2O4 nanocrystals [39]. Another reason for the ferromagnetism is the presence of defects, such as oxygen and zinc vacancies or interstitials, in the host lattice [40]. The ferromagnetic behavior of Co-doped $ZnAl_2O_4$ nanoparticles may be due to the incorporation of Co^{2+} ions into the Zn^{2+} sites and the exchange-couple interaction between Co^{2+} ions and Zn^{2+} ions [41]. As the Co concentration increases, the interaction becomes stronger, and the saturation magnetization increases.

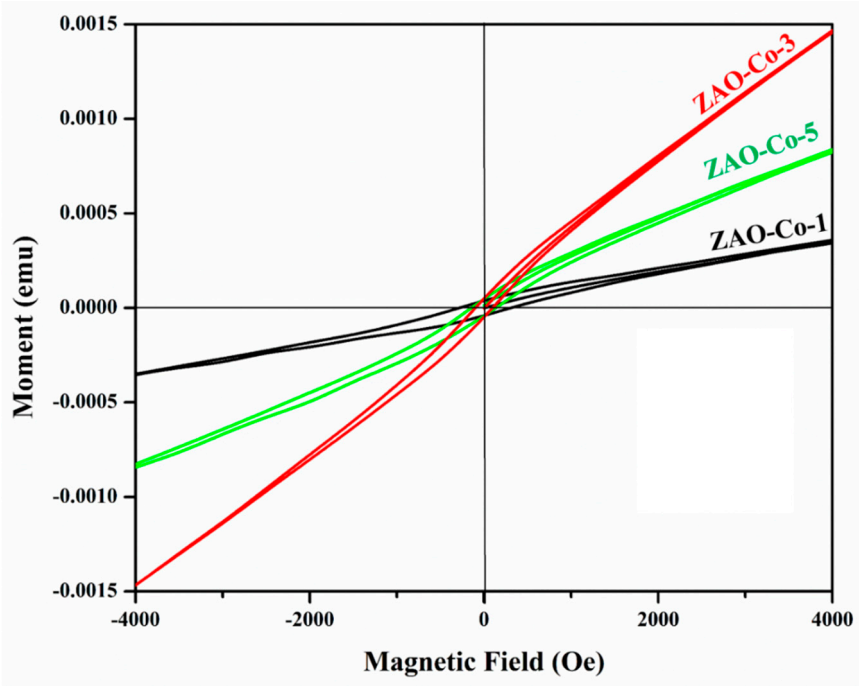


Figure 5. VSM study of Co-doped ZAO nanosheets.

Table 2. Saturation magnetization retentivity and coercivity values from VSM analysis.

Sample	Saturation Magnetization (Ms) × 10^{-3} emu	Retentivity (Mr) × 10^{-6} emu	Coercivity (Hc) Oe
ZAO-Co-1	1.11	41.73	306.10
ZAO-Co-3	4.98	54.95	104.00
ZAO-Co-5	2.68	50.34	140.70

4. Conclusions

Pure and Co-doped $ZnAl_2O_4$ were synthesized using a co-precipitation-assisted hydrothermal method at 220 °C. The pure and Co-doped $ZnAl_2O_4$ exhibited a single-phase cubic spinel structure without any secondary phases. The average crystallite size decreased with increasing Co concentration, and the lattice strain increased. XPS revealed the existence of constituent elements in the prepared sample. The energy difference (ΔE) between Co $2p_{3/2}$ and Co $2p_{1/2}$ was 15.23 eV, confirming the Co^{2+} oxidation state. TEM showed that the successful incorporation of Co ions converts the micro-hexagon structure of $ZnAl_2O_4$ to a nanoscale sheet-like structure. UV-DRS revealed a decrease in the bandgap of $ZnAl_2O_4$

with increasing Co content. The exchange couple interaction between Co^{2+} and Zn^{2+} ions enhanced the ferromagnetic behavior with increasing Co content. The successful doping of cobalt into $ZnAl_2O_4$ nanosheets can be useful in many energy-related applications.

Author Contributions: Conceptualization and writing—original draft preparation: T.R.G.; methodology, formal analysis, writing and review: B.B.; supervision, review and funding acquisition: K.Y. All authors have read and agreed to the published version of the manuscript.

Funding: This research received no external funding.

Acknowledgments: The author (Thirumala Rao) would like to thank the GMR Institute of Technology, India, for providing financial support (SEAD grant) to carry out the research work. This work was also supported by a National Research Foundation of Korea (NRF) grant funded by the Korean government [2018R1D1A1B07050330] and Technology Innovation Program (20011622, Development of Battery System applied High Efficiency Heat Control Polymer and Part Component) funded By the Ministry of Trade, Industry & Energy(MOTIE, Korea).

Conflicts of Interest: The authors declare that they have no known competing financial interests or personal relationships that could have appeared to influence the work reported in this paper.

References

1. Akika, F.Z.; Benamira, M.; Lahmar, H.; Trari, M.; Avramova, I.; Suzer, Ş. Structural and optical properties of Cu-doped $ZnAl_2O_4$ and its application as photocatalyst for Cr(VI) reduction under sunlight. *Surf. Interfaces* **2020**, *18*, 100406. [CrossRef]
2. Belyaev, A.V.; Lelet, M.I.; Kirillova, N.I.; Khamaletdinova, N.M.; Boldin, M.S.; Murashov, A.A.; Balabanov, S.S. Sol-gel synthesis and characterization of $ZnAl_2O_4$ powders for transparent ceramics. *Ceram. Int.* **2019**, *45*, 4835–4839. [CrossRef]
3. Loiko, P.; Belyaev, A.; Dymshits, O.; Evdokimov, I.; Vitkin, V.; Volkova, K.; Tsenter, M.; Volokitina, A.; Baranov, M.; Vilejshikova, E.; et al. Synthesis, characterization and absorption saturation of Co:$ZnAl_2O_4$ (gahnite) transparent ceramic and glass-ceramics: A comparative study. *J. Alloys Compd.* **2017**, *725*, 998–1005. [CrossRef]
4. Mirbagheri, S.A.; Masoudpanah, S.M.; Alamolhoda, S. Structural and optical properties of $ZnAl_2O_4$ powders synthesized by solution combustion method: Effects of mixture of fuels. *Optik* **2020**, *204*, 164170. [CrossRef]
5. Huang, S.; Wei, Z.; Wu, X.; Shi, J. Optical properties and theoretical study of Mn doped $ZnAl_2O_4$ nanoparticles with spinel structure. *J. Alloys Compd.* **2020**, *825*, 154004. [CrossRef]
6. Lahmer, M.A. The effect of Fe-doping on the electronic, optical and magnetic properties of $ZnAl_2O_4$; a first-principles study. *Comput. Condens. Matter* **2019**, *20*, e00387. [CrossRef]
7. Yong, X.; Ping, F.; Baohua, Z.; Juan, G.; Lin, Z.; Xuehua, W. Optical properties of transparent $ZnAl_2O_4$ ceramics: A new transparent material prepared by spark plasma sintering. *Mater. Lett.* **2014**, *123*, 142–144. [CrossRef]
8. Bhavani, P.; Manikandan, A.; Paulraj, P.; Dinesh, A.; Durka, M.; Antony, S.A. Okra (Abelmoschus esculentus) Plant Extract-Assisted Combustion Synthesis and Characterization Studies of Spinel $ZnAl_2O_4$ Nano-Catalysts. *J. Nanosci. Nanotechnol.* **2018**, *18*, 4072–4081. [CrossRef]
9. Cornu, L.; Gaudon, M.; Jubera, V. $ZnAl_2O_4$ as a potential sensor: Variation of luminescence with thermal history. *J. Mater. Chem. C* **2013**, *1*, 5419–5428. [CrossRef]
10. Kumar, K.; Ramamoorthy, K.; Koinkar, P.M.; Chandramohan, R.; Sankaranarayanan, K. A novel way of modifying nano grain size by solution concentration in the growth of $ZnAl_2O_4$ thin films. *J. Nanopart. Res.* **2007**, *9*, 331–335. [CrossRef]
11. Motloung, S.V.; Kumari, P.; Koao, L.F.; Motaung, T.E.; Hlatshwayo, T.T.; Mochane, M.J. Effects of annealing time on the structure and optical properties of $ZnAl_2O_4$/ZnO prepared via citrate sol-gel process. *Mater. Today Commun.* **2018**, *14*, 294–301. [CrossRef]
12. Cornu, L.; Duttine, M.; Gaudon, M.; Jubera, V. Luminescence switch of Mn-Doped $ZnAl_2O_4$ powder with temperature. *J. Mater. Chem. C* **2014**, *2*, 9512–9522. [CrossRef]
13. Denisov, I.A.; Volk, Y.V.; Malyarevich, A.M.; Yumashev, K.V.; Dymshits, O.S.; Zhilin, A.A.; Kang, U.; Lee, K.H. Linear and nonlinear optical properties of cobalt-doped zinc aluminum glass ceramics. *J. Appl. Phys.* **2003**, *93*, 3827–3831. [CrossRef]
14. Rani, G. Annealing effect on the structural, optical and thermoluminescent properties of $ZnAl_2O_4$:Cr^{3+}. *Powder Technol.* **2017**, *312*, 354–359. [CrossRef]
15. Kumar, M.; Gupta, S.K. An insight into optical spectroscopy of intense green emitting $ZnAl_2O_4$:Tb^{3+} nanoparticles: Photo, thermally stimulated luminescence and EPR study. *J. Lumin.* **2015**, *168*, 151–157. [CrossRef]
16. Kumari, P.; Dwivedi, Y. Structural and photophysical investigations of bright yellow emitting Dy: $ZnAl_2O_4$ nanophosphor. *J. Lumin.* **2016**, *178*, 407–413. [CrossRef]
17. Belyaev, A.; Basyrova, L.; Sysoev, V.; Lelet, M.; Balabanov, S.; Kalganov, V.; Mikhailovski, V.; Baranov, M.; Stepanidenko, E.; Vitkin, V.; et al. Microstructure, doping and optical properties of Co^{2+}:$ZnAl_2O_4$ transparent ceramics for saturable absorbers: Effect of the ZnF_2 sintering additive. *J. Alloys Compd.* **2020**, *829*, 154514. [CrossRef]
18. Tsai, M.T.; Chang, Y.S.; Huang, I.B.; Pan, B.Y. Luminescent and structural properties of manganese-doped zinc aluminate spinel nanocrystals. *Ceram. Int.* **2013**, *39*, 3691–3697. [CrossRef]

19. Ragupathi, C.; Kennedy, L.J.; Vijaya, J.J. A new approach: Synthesis, characterization and optical studies of nano-zinc aluminate. *Adv. Powder Technol.* **2014**, *25*, 267–273. [CrossRef]
20. Basavaraju, N.; Priolkar, K.R.; Gourier, D.; Sharma, S.K.; Bessière, A.; Viana, B. The importance of inversion disorder in the visible light induced persistent luminescence in Cr^{3+} doped AB_2O_4 (A = Zn or Mg and B = Ga or Al). *Phys. Chem. Chem. Phys.* **2015**, *17*, 1790–1799. [CrossRef]
21. Parya, T.K.; Bhattacharyya, R.K.; Banerjee, S.; Adhikari, U.B. Co-precipitated $ZnAl_2O_4$ spinel precursor as potential sintering aid for pure alumina system. *Ceram. Int.* **2010**, *36*, 1211–1215. [CrossRef]
22. Zou, L.; Li, F.; Xiang, X.; Evans, D.G.; Duan, X. Self-generated Template Pathway to High-Surface-Area Zinc Aluminate Spinel with Mesopore Network from a Single-Source Inorganic Precursor. *Chem. Mater.* **2006**, *18*, 5852–5859. [CrossRef]
23. Zawadzki, M. Synthesis of nanosized and microporous zinc aluminate spinel by microwave assisted hydrothermal method (microwave–hydrothermal synthesis of $ZnAl_2O_4$). *Solid State Sci.* **2006**, *8*, 14–18. [CrossRef]
24. Tangcharoen, T.; Thienprasert, J.; Kongmark, C. Optical properties and versatile photocatalytic degradation ability of MAl_2O_4 (M = Ni, Cu, Zn) aluminate spinel nanoparticles. *J. Mater. Sci. Mater. Electron.* **2018**, *29*, 8995–9006. [CrossRef]
25. Chaudhary, A.; Mohammad, A.; Mobin, S.M. Facile synthesis of phase pure ZnAl2O4 nanoparticles for effective photocatalytic degradation of organic dyes. *Mater. Sci. Eng. B* **2018**, *227*, 136–144. [CrossRef]
26. Wu, X.; Wei, Z.; Chen, X.; Wang, X.; Yang, H.; Jiang, J. Optical properties and microstructure of Ni doped $ZnAl_2O_4$ nanopowders synthesized by sol–gel method. *J. Mater. Sci. Mater. Electron.* **2015**, *26*, 6606–6611. [CrossRef]
27. Komahal, F.F.; Nagabhushana, H.; Basavaraj, R.B.; Darshan, G.P.; Prasad, B.D. Solvothermal synthesis and luminescent properties of hierarchical flowerlike $ZnAl_2O_4$:Ho^{3+} microstructures. *Opt. Mater.* **2018**, *84*, 536–544. [CrossRef]
28. Pan, Q.; Ye, S.; Yang, D.; Qiu, J.; Dong, G. Multifunctional magnetic-fluorescent Ni-doped $ZnAl_2O_4$ nanoparticles with second biological NIR window fluorescence. *Mater. Res. Bull.* **2017**, *93*, 310–317. [CrossRef]
29. Singh, V.; Singh, N.; Pathak, M.S.; Dubey, V.; Singh, P.K. Annealing effects on the luminescence properties of Ce doped $ZnAl_2O_4$ produced by combustion synthesis. *Optik* **2018**, *155*, 285–291. [CrossRef]
30. Maity, G.; Maji, P.; Sain, S.; Das, S.; Kar, T.; Pradhan, S.K. Microstructure, optical and electrical characterizations of nanocrystalline $ZnAl_2O_4$ spinel synthesized by mechanical alloying: Effect of sintering on microstructure and properties. *Phys. E Low Dimens. Syst. Nanostruct.* **2019**, *108*, 411–420. [CrossRef]
31. Parthasarathy, S.; Nandhini, V.; Jeyaprakash, B.G. Improved sensing response of photo activated ZnO thin film for hydrogen peroxide detection. *J. Colloid Interface Sci.* **2016**, *482*, 81–88. [CrossRef]
32. Dallaeva, D.S.; Bilalov, B.A.; Gitikchieva, M.A.; Kardashova, G.D.; Safaraliev, G.K.; Tománek, P.; Škarvada, P.; Smith, S. Structural properties of Al_2O_3/AlN thin film prepared by magnetron sputtering of Al in HF-activated nitrogen plasma. *Thin Solid Films* **2012**, *526*, 92–96. [CrossRef]
33. Shang-Pan, H.; Zhi-Qiang, W.; Xiao-Juan, W.; Ji-Wen, S. Optical properties of Cr doped $ZnAl_2O_4$ nanoparticles with Spinel structure synthesized by hydrothermal method. *Mater. Res. Express* **2020**, *7*, 015025. [CrossRef]
34. Wang, C.C.; Liu, M.; Man, B.Y.; Chen, C.S.; Jiang, S.Z.; Yang, S.Y.; Gao, X.G.; Xu, S.C.; Hu, B.; Sun, Z.C.; et al. Role of cobalt in room-temperature ferromagnetic Co-doped ZnO thin films. *AIP Adv.* **2012**, *2*, 012182. [CrossRef]
35. Rahman, A.; Charoo, M.S.; Jayaganthan, R. Structural, optical and photocatalytic properties of zinc aluminate spinel nanoparticles. *Mater. Technol.* **2015**, *30*, 168–176. [CrossRef]
36. Duan, X.; Yuan, D.; Yu, F. Cation Distribution in Co-Doped $ZnAl_2O_4$ Nanoparticles Studied by X-ray Photoelectron Spectroscopy and 27Al Solid-State NMR Spectroscopy. *Inorg. Chem.* **2011**, *50*, 5460–5467. [CrossRef] [PubMed]
37. Skoda, D.; Urbanek, P.; Sevcik, J.; Munster, L.; Nadazdy, V.; Cullen, D.A.; Bazant, P.; Antos, J.; Kuritka, I. Colloidal cobalt-doped ZnO nanoparticles by microwave-assisted synthesis and their utilization in thin composite layers with MEH-PPV as an electroluminescent material for polymer light emitting diodes. *Org. Electron.* **2018**, *59*, 337–348. [CrossRef]
38. Xu, X.; Cao, C. Structure and ferromagnetic properties of Co-doped ZnO powders. *J. Magn. Magn. Mater.* **2009**, *321*, 2216–2219. [CrossRef]
39. Rao, C.N.R.; Deepak, F.L. Absence of ferromagnetism in Mn- and Co-doped ZnO. *J. Mater. Chem.* **2005**, *15*, 573–578. [CrossRef]
40. Siddheswaran, R.; Mangalaraja, R.V.; Gómez, M.E.; Avila, R.E.; Jeyanthi, C.E. Room temperature ferromagnetism in combustion synthesized nanocrystalline Co, Al co-doped ZnO. *J. Alloys Compd.* **2013**, *581*, 146–149. [CrossRef]
41. Basith, N.M.; Vijaya, J.J.; Kennedy, L.J.; Bououdina, M.; Jenefar, S.; Kaviyarasan, V. Co-Doped ZnO Nanoparticles: Structural, Morphological, Optical, Magnetic and Antibacterial Studies. *J. Mater. Sci. Technol.* **2014**, *30*, 1108–1117. [CrossRef]